AIP Advances

RESEARCH ARTICLE | DECEMBER 05 2025

Optimizing pyroelectric x-ray detectors for synchrotron applications

S. R. Kane ; R. W. Whatmore ; P. K. Jha ; P. K. Mehta

Check for updates

AIP Advances 15, 125309 (2025)
https://doi.org/10.1063/5.0301701

View Online
Export Citation

Articles You May Be Interested In

Experimental setup to measure thermal waves generated by X-ray absorption using pyroelectric sensor

Rev. Sci. Instrum. (March 2019)

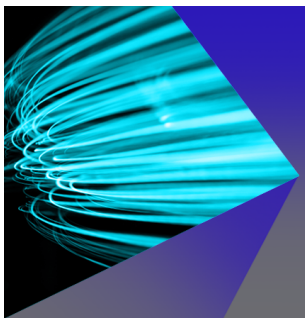
Advanced pyroelectric materials for high-performance infrared detection: Design, simulation, and optimization using finite element method in COMSOL multiphysics

AIP Conf. Proc. (August 2025)

Enhanced pyroelectric sensitivity using ferroelectric active mode detection

Appl. Phys. Lett. (March 2007)

08 December 2025 10:51:56



AIP Advances

Special Topics Now Online

Learn More

AIP Publishing

AIP Publishing

Optimizing pyroelectric x-ray detectors for synchrotron applications

Cite as: AIP Advances 15, 125309 (2025); doi: 10.1063/5.0301701
Submitted: 20 October 2025 • Accepted: 17 November 2025 •
Published Online: 5 December 2025

View Online Export Citation CrossMark

S. R. Kane,[1,a] R. W. Whatmore,[2] P. K. Jha,[3] and P. K. Mehta[3]

AFFILIATIONS

[1] Accelerator Physics and Synchrotrons Utilization Division, Raja Ramanna Centre for Advanced Technology, Indore 452013, India
[2] Department of Materials, Faculty of Engineering, Imperial College London, London SW7 2AZ, United Kingdom
[3] Department of Physics, The M S University of Baroda, Vadodara 390002, India

[a] **Author to whom correspondence should be addressed:** rksanjiv@rrcat.gov.in

ABSTRACT

This study presents a comprehensive investigation of pyroelectric detectors for high-energy x-ray detection. We compare three high-performance pyroelectric materials ($LiTaO_3$, $LiNbO_3$, and triglycine sulfate) in two geometries, thermally coupled and uncoupled, and contrasting current with conventional voltage amplifier designs. The results obtained using 17 keV synchrotron radiation demonstrate that current amplification significantly outperforms voltage follower configurations, achieving responsivity values of up to 10^5 V/W with substantially improved signal-to-noise ratios. Of the three materials tested, triglycine sulfate exhibits superior sensitivity when used in thicker formats (specific detectivity D^* ~ 7.60×10^7 cm $Hz^{1/2}$ W^{-1}), although $LiTaO_3$ offers better thermal stability for practical applications. Further optimization through thickness reduction of $LiTaO_3$ crystals in the range of 500–100 μm yielded substantial improvements in D^*, with the thinnest crystals achieving D^* values of ~1.1×10^8 cm $Hz^{1/2}$ W^{-1} in uncoupled geometry, which maximizes thermal isolation and temperature rise per unit-absorbed power. These results validate our theoretical models, which predict performance enhancements through optimal thermal management and amplification strategies. This establishes new benchmarks for pyroelectric-based x-ray detection.

© 2025 Author(s). All article content, except where otherwise noted, is licensed under a Creative Commons Attribution (CC BY) license (https://creativecommons.org/licenses/by/4.0/). https://doi.org/10.1063/5.0301701

08 December 2025 10:51:56

I. INTRODUCTION

A range of modern science (e.g., high energy synchrotrons) and medical facilities require sensors capable of x-radiation detection and measurement with high sensitivity and precision.[1,2] Conventional x-ray detectors are well established: ionization chambers excel in transmission-mode flux monitoring with excellent linearity and stability, silicon drift detectors (SDDs) provide outstanding energy resolution (123–135 eV) for spectroscopic measurements, and silicon photodiodes offer fast response for timing applications. However, each faces specific limitations: ionization chambers require space in the beam path and high-voltage systems, SDDs need active cooling and can saturate at very high flux (>10^6 cps), and photodiodes have a limited dynamic range.[3,4]

These limitations motivate exploration of alternative detection mechanisms. Pyroelectric detectors,[5] traditionally employed for infrared and thermal imaging, have recently emerged as a possible solution[6] for x-ray detection. Pyroelectric detectors offer complementary capabilities to other detectors. As they are thermal (bolometric) detectors, they potentially offer broadband spectral response without energy discrimination. They are inherently radiation hard and should be high-flux tolerant. They are compact in size (relevant for reflection geometries), require no cooling, and are of low cost. Their strengths are particularly relevant for high-flux beam monitoring in the context of synchrotron radiation where conventional detectors may saturate and experimental setups prioritize simplicity, cost-effectiveness, and maintenance-free operation. Their relatively long thermal time constants (100's of milliseconds) mean that they integrate detectors that are insensitive to the time-structure of the synchrotron radiation beam. Pyroelectric sensors are relatively insensitive to ambient temperature changes (lithium tantalate pyroelectric sensors, for example, have a response that changes little between −40 and 100 °C). Interestingly, although pyroelectric detectors are "thermal detectors," their frequency response

© Author(s) 2025

characteristics mean that they are insensitive to slow changes in ambient temperature that occur over 10's of seconds. These characteristics of environmental robustness and low cost mean that pyroelectric infrared (PIR) sensors are widely used in external applications such as motion-operated light switches and "smart" doorbell cameras.[5] All these properties mean that pyroelectric sensors offer an interesting alternative to more conventional approaches to x-ray detection and monitoring. In this context, they are not intended to replace conventional detectors but to address specific measurement scenarios where traditional detectors face practical constraints.

The evolution of pyroelectric detection can be traced back to 1938, when Ta first demonstrated infrared (IR) sensing using tourmaline crystals.[7] Owing to their simplicity, pyroelectric detectors offer a cost-effective and flexible solution for broadband radiation detection, including infrared sensing[5,8] and thermal imaging,[9,10] but there are limited studies for their use in the detection of x-ray and gamma ray photons and x-ray spectroscopy.[11] Hester *et al.*[12] first explored using the pyroelectric effect in PZT ceramics for gamma ray dosimetry and showed that it was feasible to detect high-energy photons in this way. Kremenchugskii and Strakovskaya[13] and Carvalho *et al.*[14] demonstrated the use of this effect in a dosimeter. Sakamoto *et al.*[15] demonstrated the linearity of the pyroelectric response to 120–300 kVp x-ray intensity in PZT-PEEK composites. Recent studies also explored the use of pyroelectric effect for x-ray generation via electron acceleration in vacuum,[16,17] neutron production through deuteron bombardment,[18] and energy harvesting.[19] Recently, Kane *et al.*[11] demonstrated that the pyroelectric effect could be used in x-ray spectroscopy. None of the work cited above had attempted to quantify the signal-to-noise ratio that could be obtained by using a pyroelectric detector for x-ray detection.

Recently, a study by Kane *et al.*[6] demonstrated $LiTaO_3$ (LT), $LiNbO_3$ (LN), and triglycine sulfate $(NH_2CH_2COOH)_3{\cdot}H_2SO_4$ (TGS) detectors bonded to a copper substrate and equipped with a voltage-mode readout amplifier. The voltage responsivities (R_v^V), noise equivalent powers (NEPs), and specific detectivities (D^*) for 17 keV x rays were quantified and reported for the first time. However, theoretical modeling showed that the performances of the detectors depended critically on both the thermal coupling between the crystal and its substrate and the amplifier scheme used to extract the signal. In this study, we have systematically investigated the interplay between thermal design, amplifier architecture, and material choice for x-ray pyroelectric detection. Specifically, we evaluate LT, LN, and TGS configured in two distinct thermal geometries, coupled (crystal bonded to a conductive copper substrate) and uncoupled (corner-supported over a copper substrate with an air gap), to reduce thermal leakage. Concurrently, we also evaluate two amplifier schemes: voltage-mode readout, which is straightforward but susceptible to capacitive signal loss, and current-mode (transimpedance) readout, which uses a slightly more complex circuit to directly measure pyroelectric current. Our results provide insights into how pyroelectric detector performance can be optimized for high-flux x-ray applications and have demonstrated for the first time that pyroelectric detectors can produce D^* values in excess of 10^8 cm $Hz^{1/2}$ W^{-1} when used for x-ray detection.

II. PYROELECTRIC DEVICES

Pyroelectric materials possess a spontaneous electric polarization that varies with temperature. When configured as thin, electrode-coated plates ("elements"), they act as dynamic capacitors that release free charges when absorbed radiation energy induces changes in element temperature with time. Pyroelectric detectors operate effectively at ambient temperature and possess the attractive characteristic that they can respond to any wavelength of radiation, as long as the radiation energy can be absorbed in the active pyroelectric element and dissipated as heat to cause a temperature change in the element. Very small temperature changes in the element of $<10^{-6}$ K are detectable.

The pyroelectric current I_p is given by

$$I_p = pA\frac{dT}{dt}, \tag{1}$$

where p is the pyroelectric coefficient (in units of C m^{-2} K^{-1}), A is the electrode area, and dT/dt is the rate of change of element temperature. This current is typically very small (in the pA range or less), requiring amplification before it can be processed or measured.[21,22] The amplifier can operate in either voltage-mode or in current-mode.[23,24]

The pre-amplification stage of the readout electronics is a critical component in pyroelectric detector systems, as it significantly influences the overall performance by minimizing electronic noise. To achieve optimal performance, special care must be taken in the selection of components or circuit design to ensure that the electronic noise remains below the dielectric noise of the pyroelectric element. Two principal readout schemes are commonly used:

(1) Voltage amplifier: The basic functional diagram of a voltage amplifier is shown in Fig. 1. A high-impedance field-effect transistor (FET) is directly connected to the pyroelectric element, which is in parallel with a high value resistor R_p. The signal is manifested as a voltage across the device capacitance. This scheme is compact and simple but susceptible to capacitive loading (such as interconnections), which can attenuate the signal especially at high frequencies or with large input capacitance C_E.[5,25–27] The design has an electrical time constant associated with it, given by $\tau_E = R_p(C_p + C_E)$,

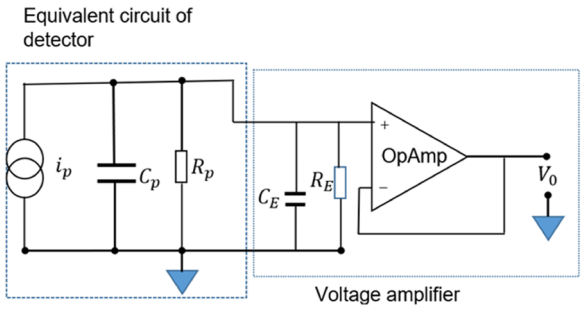


FIG. 1. The electrical structure of pyroelectric element with voltage amplifier.

08 December 2025 10:51:56

© Author(s) 2025

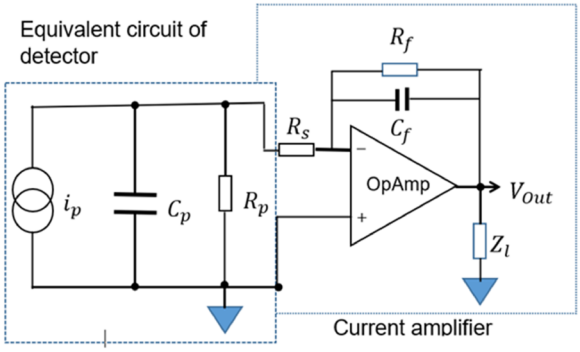


FIG. 2. The electrical structure of pyroelectric element with current amplifier.

which will produce an electrical turn-over frequency, given by $f_E = 1/(2\pi\tau_E)$.

(2) Current amplifier: With advances in electronics, the introduction of low-input-bias and low-noise integrated circuits (ICs) enabled the adoption of trans-impedance current amplifiers (TIAs), as shown in Fig. 2, which many researchers have found to be superior for the application.[23,24,28,29] The transimpedance amplifier (TIA) configuration is used to convert the pyroelectric current directly into a voltage using a feedback resistor. This scheme improves signal fidelity by bypassing the capacitive limitations of voltage-mode and allows accurate measurement of I_p.[8,9]

The differences in amplifier characteristics have been discussed in detail elsewhere,[23,24] but generally, voltage amplifiers produce slightly lower noise equivalent powers (NEPs) than current amplifiers, but current amplifiers have more-freedom associated with the design of electrical time constants and are less susceptible to stray capacitances between the detector element and amplifier, especially where the element needs to be physically separated from the amplifier, as can be the case in x-ray detection.

Detector performance is characterized using several key figures of merit:

(a) Voltage responsivity R_v^V: Pyroelectric sensor responsivity (whether with a voltage or current amplifier) to sinusoidally modulated input radiation is defined as the ratio of the root mean square (rms) value of the electrical output signal to the rms value of the input radiation power.[5,24,26,30,31] The units of responsivity are volts per watt (V/W). In this article, we are using the following notations: R_v^V for voltage amplifier configuration, where superscript "V" denotes the voltage amplifier; R_v^i for current amplifier (*TIA*) configuration, where superscript "i" denotes the current amplifier; and $R_v^{V,i}$ when discussing both configurations together, where this notation indicates that the discussion or equation applies to both amplifier types.

The formula for calculating responsivity to radiation illuminating the detector at angular frequency ω when a voltage amplifier is used is

$$R_v^V = \frac{\omega\eta R_T A p}{G_T\sqrt{(1+\tau_T^2\omega^2)}\sqrt{(1+\tau_E^2\omega^2)}}, \tag{2}$$

where p is the pyroelectric coefficient of the material used, η is the absorption efficiency of the detector, and A is its area. G_T represents the thermal conductance between the detector element and its surroundings. The thermal and electrical time constants, τ_T and τ_E, are critical parameters that determine the frequency response characteristics of the pyroelectric detector. Both types of amplifiers are influenced by τ_T and τ_E, but the parameters that define the electrical time constant differ in each case. In the case of a voltage amplifier, the electrical time constant is $\tau_E = (R_p \| R_E) \times (C_p + C_E)$, whereas in a current amplifier, $\tau_E = (R_f) \times (C_f)$. The article by Whatmore and Ward[24] explains in detail how the well-known theories describing the way an operational amplifier (OPAMP) works can be used to model the voltage responsivity when a current amplifier is used (R_v^i). The current-to-voltage transfer function (Ξ) is given as

$$\Xi = \frac{Z_f}{\left[1 + [A_{OL}\beta]^{-1}\right]}, \tag{3}$$

where Z_f is the impedance of the feedback RC network, A_{OL} is the open loop gain, and β is the feedback of the OPAMP, given as $\beta = \frac{Z_f}{Z_f + Z_i}$. For an ideal OPAMP, $A_{OL} \to \infty$, implying $\Xi \approx Z_f$. For real-world amplifiers, A_{OL} is not infinite, and β varies with frequency. By retaining Ξ, the model accounts for the following: (1) gain roll-off: at high frequencies, A_{OL} decreases, reducing Ξ and limiting responsivity; (2) phase stability: the $\left(1 + [A_{OL}\beta]^{-1}\right)$ term prevents oscillations by ensuring the amplifier operates within its stable bandwidth; (3) frequency-dependent errors: non-ideal A_{OL} introduces deviations from the ideal Z_f approximation, which are corrected by Ξ. This approach avoids oversimplifications and ensures the model remains valid for practical amplifier designs, where non-idealities significantly impact responsivity and noise. Thus, Ξ bridges idealized theory and real-world electronics, enabling reliable optimization of pyroelectric detectors for applications requiring precise sensitivity and stability.

(b) Noise equivalent power (NEP) (W $Hz^{-1/2}$): Noise Equivalent Power (NEP) is a critical parameter as it quantifies a detector's sensitivity. It is defined as the incident power required to achieve a signal-to-noise ratio (SNR) of unity in a 1 Hz output bandwidth. A lower NEP indicates higher sensitivity, enabling detection of weaker signals.[31,32] For pyroelectric detectors, NEP is influenced by both material properties and readout electronics. The NEP of a pyroelectric detector can be calculated using the following formula for a given response voltage, noise voltage, and incident energy:

$$NEP = \Delta v_n / R_v^{V,i}, \tag{4}$$

where Δv_n represents the rms noise voltage and $R_v^{V,i}$ is the voltage responsivity for the voltage or current amplifier, whichever is being used.

The dominant noise sources depend on the following amplifier configurations: voltage amplifier (source follower): noise is usually dominated by the amplifier's voltage noise

08 December 2025 10:51:56

© Author(s) 2025

due to high source impedance, although the Johnson noise associated with the dielectric loss of the pyroelectric capacitor can dominate, especially at higher frequencies;[26,33] current amplifier (transimpedance amplifier, TIA): Johnson noise from the feedback resistor (R_f) and voltage noise from the amplifier contribute significantly, particularly at high detector impedances.[24,34] However, it is hard to generalize, and the noise must be calculated in each specific case for the device engineer to be sure which one will dominate.

(c) Specific detectivity (D^*) quantifies a pyroelectric detector's ability to detect weak signals amidst noise. It is defined as the reciprocal of the Noise Equivalent Power (NEP) normalized by the square root of the detector area (A) and measurement bandwidth (Δf). D^* is expressed as $D^* = \sqrt{A \times \Delta f}/NEP$, typically in units of cm $Hz^{1/2}$ W^{-1} or "Jones." This normalization enables direct performance comparison between detectors of varying dimensions. Higher D^* values indicate a superior detector design. The highest detectivity reported in the IR region for a 2 × 2 mm^2 $LiTaO_3$ detector is of the order of 4×10^8 cm $Hz^{1/2}$ W^{-1} @ 10 Hz.[35,36] Recently, Kane *et al.* reported the detectivity of a 500 μm thick LT crystal of a linear size of 5 × 5 mm^2 in the hard x-ray (17 keV) region generated by synchrotron radiation of the order of 10^7 cm $Hz^{1/2}$ W^{-1}.[6]

Thermal design plays a crucial role in determining detector performance. The thermal time constant ($\tau_T = H_T/G_T$), where H_T is the heat capacity and G_T is the thermal conductance, dictates the detector's temporal response and sensitivity. In the "coupled" geometries used in this project, crystals are bonded to copper substrates using silver epoxy, which maximizes heat dissipation and increases G_T. In the "uncoupled" geometries, thermal contact is minimized through corner-supported mounting of the detector crystals and by having an air-gap under the element. In this case, thermal isolation is enhanced, reducing G_T. The coupled design is a robust construction but has reduced thermal time constants (τ_T) through the rapid heat transfer to the substrate.[21,37,38] On the other hand, the uncoupled configuration increases sensitivity by localizing and maximizing temperature changes within the element,[39–41] but at the expense of a slightly more complex, less-robust construction.

Understanding and optimizing this interplay between thermal configuration, amplifier architecture, and material properties are essential for designing high-performance pyroelectric detectors for high-flux, high-energy x-ray applications.

III. EXPERIMENTAL

A. Experimental methods and detector fabrication

The experimental setup and fabrication of the coupled geometry detector design are illustrated in Fig. 3(a) and were explained in a prior work.[6,42] For this work also, we have utilized optical-grade Z-cut single-crystal LT with different thickness ranging from 0.1 to 0.5 mm and LN with a thickness of 0.5 mm, as well as b-axis oriented TGS crystals with a thickness of 0.35 mm. In case of coupled geometry, the pyroelectric crystals were coated with silver paste electrodes ~100 μm thick and bonded to 1 mm oxygen-free copper backing plates using silver-loaded epoxy for mechanical support and thermal dissipation.

In the uncoupled geometry, to reduce thermal contact, 5 × 5 mm^2 crystal elements were corner-supported using four cylindrical silver epoxy dots (1 mm diameter) instead of full-area bonding. A 4 mm circular hole was machined through the copper

08 December 2025 10:51:56

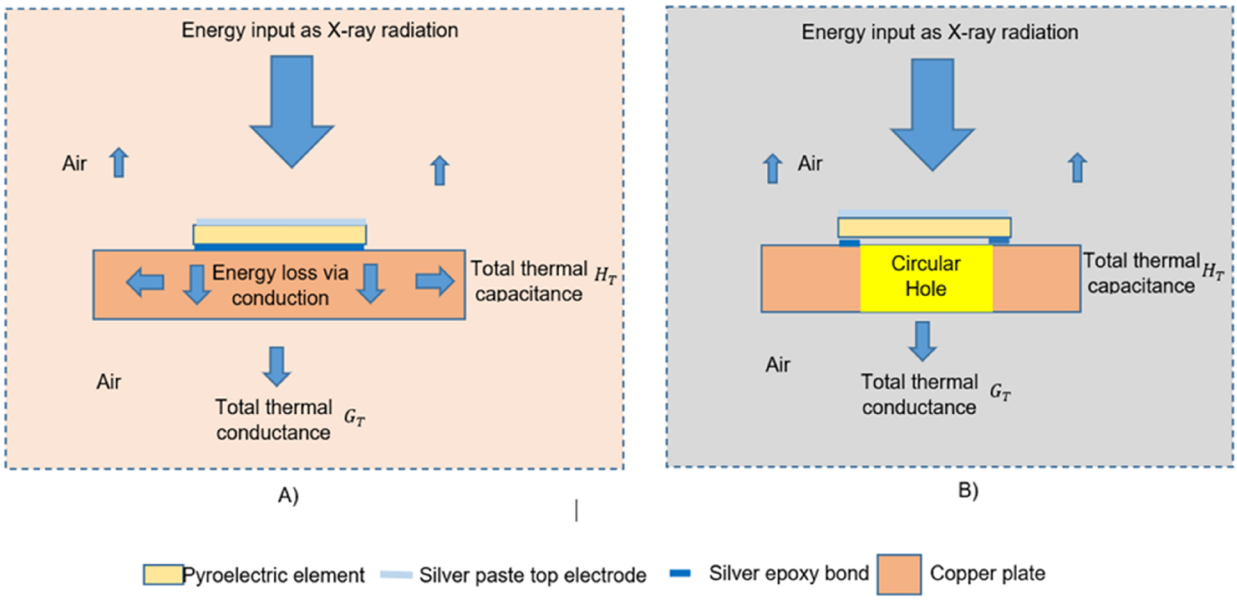


FIG. 3. Basic thermal structure of pyroelectric devices made from bulk pyroelectric material in coupled (A) and uncoupled (B) geometry.

© Author(s) 2025

TABLE I. Thermal properties, electrical time constants, and corresponding frequencies for the pyroelectric crystals in different geometries and thicknesses.

Pyroelectric element	$LiNbO_3$	TGS	$LiTaO_3$	$LiTaO_3$	$LiTaO_3$	$LiTaO_3$	Unit
Thickness	500	350	100	200	300	500	μm
τ_E	0.042	0.054	0.11	0.058	0.042	0.049	s
f_E	3.76	2.97	1.50	2.75	3.79	3.24	Hz
Coupled thermal parameters							
H_T	3.60×10^{-2}	1.82×10^{-2}	1.05×10^{-2}	1.90×10^{-2}	2.65×10^{-2}	4.13×10^{-2}	J K^{-1}
G_T	1.87×10^{-1}	7.55×10^{-2}	2.25×10^{-1}	2.01×10^{-1}	1.82×10^{-1}	2.10×10^{-1}	W K^{-1}
τ_T	0.193	0.241	0.047	0.095	0.146	0.197	s
f_T	0.827	0.660	3.410	1.684	1.093	0.809	Hz
Uncoupled thermal parameters							
H_T	4.25×10^{-2}	2.37×10^{-2}	1.05×10^{-2}	1.98×10^{-2}	2.92×10^{-2}	4.70×10^{-2}	J K^{-1}
G_T	1.78×10^{-2}	8.45×10^{-2}	8.65×10^{-3}	1.19×10^{-2}	1.40×10^{-2}	1.65×10^{-2}	W K^{-1}
τ_T	2.388	0.280	1.214	1.664	2.086	2.851	s
f_T	0.067	0.567	0.131	0.096	0.076	0.056	Hz

plate beneath the crystal to create an air-gap and minimize conductive heat loss, enhancing thermal isolation. The thermal characteristics of each structure were modeled using COMSOL software, as described elsewhere.[6] The resulting values of G_T and H_T are given in Table I, together with the values of τ_T and the values of the turnover frequencies corresponding with these, given by $f_T = 1/(2\pi\tau_T)$. It can be seen that the values of f_T for most of the configurations explored are well below the measurement range of 2–100 Hz. The exceptions are the 100 and 200 μm thick $LiTaO_3$ crystals, for which we predict f_T values of 3.4 and 1.7 Hz, respectively. This point will be discussed further below.

Experiments were conducted at the Angle-Dispersive X-Ray Diffraction (ADXRD) beamline[43] of the Indus-2 synchrotron, a third-generation facility[44] providing tunable x rays (5–25 keV) with a photon flux of ~10^{10} photons/s. A monochromatic x-ray energy of 17 keV with an incident x-ray power of 0.30 μW was maintained throughout all measurements. The x-ray beam was precisely focused to a size of 3 × 3 mm^2 using the beamline's pre- and post-mirror systems. Beam chopping was performed using the mechanical chopper system at frequencies ranging from 1.8 to 80 Hz to modulate the x-ray flux for pyroelectric response measurements. Ambient temperature was maintained at 25 ± 2 °C throughout the experiments. Beam intensity stability was monitored using an upstream ionization chamber.

The pulsed temporal structure of synchrotron radiation (bunch frequency ~550 MHz for Indus-2) is effectively averaged by the pyroelectric detector's thermal time constants (1–100 ms), eliminating concerns about pulse-counting corrections typically required for photon-counting detectors. This thermal averaging ensures that the high-frequency pulse structure of synchrotron radiation does not affect the detector response, which is governed by the thermal time constants rather than the photon arrival statistics.

By modulating the x-ray flux at frequencies from 1.8 to 80 Hz, we characterized responsivity ($R_v^{V,i}$), noise equivalent power (NEP), and detectivity (D^*) across both geometries and amplifier types. To ensure the reliability and repeatability of our measurements, we performed multiple successive measurements on the same device under identical conditions. Specifically, each measurement of responsivity ($R_v^{V,i}$) and noise was repeated at least five times over a period of several hours, with the device maintained in a stable environment to minimize external influences. Noise characterization was carried out using both coupled and uncoupled geometries, with a current amplifier and a Rohde & Schwarz (FPL1003) spectrum analyzer. Detailed noise measurement methodologies are described in detail in a prior work.[6]

B. Preamplifier design

The voltage amplifier design was discussed in detail previously.[6] Table I lists the electrical time constants τ_E, and the corresponding turn-over frequencies f_E, for each configuration. It can be seen that most of the values of f_E for the voltage amplifier are at the lower-end, but still within the measurement frequency range of 2–100 Hz. This has an effect on the results, which will be discussed below.

The core of our TIA design (Fig. 2) is the ADA4530-1 (Analog Devices, Inc.) electrometer, chosen for its ultra-low input bias current (±20 fA) and integrated guard buffer. The guard buffer isolates input pins from PCB leakage currents, ensuring high-precision signal acquisition. A precision feedback resistor (R_f = 10 GΩ; 5% tolerance; 200 ppm thermal coefficient) and capacitor (C_f = 10 pF; NP0-grade ceramic) set the transimpedance gain and bandwidth, with the electrical turnover frequency defined as $f_E = \frac{1}{2\pi R_f C_f}$.

This configuration achieves a turnover frequency of 1.6 Hz, just below the measurement frequency range (1.8–80 Hz). The ADA4530-1 output is further amplified by an ADA8220 instrumentation amplifier (total gain = ×100). The detailed circuit diagram of this current amplifier is given in the supplementary material. Rigorous PCB guarding, grounding,[45] and EMI/RFI shielding (via a metal enclosure) suppress external noise sources. The amplifier's

08 December 2025 10:51:56

© Author(s) 2025

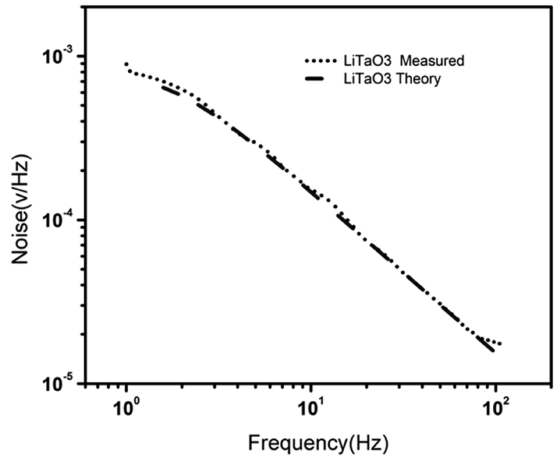


FIG. 4. Current amplifier noise values measured from 1 to 100 Hz for a device with an LT crystal (500 μm thick) active element, compared with the theoretically calculated values.

leakage current (0.04 pA) and equivalent input noise current (0.07 fA $Hz^{-1/2}$) were used in the theoretical calculations.

Figure 4 compares the theoretical and measured noise spectra for an LT detector in coupled geometry for the current amplifier. The noise for all the pyroelectric material was measured using the Rohde & Schwarz (FPL1003) spectrum analyzer for both the geometries. The detailed procedure for the noise measurement was explained previously.[6] The excellent agreement between the experimental data and the Johnson–Nyquist noise theory validates our noise model, confirming the accuracy of the theoretical predictions.

In this work, we measured responsivities (R_v^i and R_v^V) and device noises as functions of frequency from 2 to 100 Hz for coupled and uncoupled geometries for (1) pyroelectric materials of a thickness of 500 μm for LT and LN, and 350 μm for TGS and (2) various thicknesses of LT, i.e., 100, 200, 300, and 500 μm. The responsivities, NEP, and D^* values were also calculated using the models described by Whatmore and Ward,[24] and the thermal and electrical time constants are presented in Table I. The experimental results are compared with these predictions throughout.

IV. RESULTS

A. Responsivity

1. For different pyroelectric materials

Figure 5 presents the current-amplifier responsivities (R_v^i) of TGS-, LT-, and LN-based devices across different chopping frequencies, while Fig. 6 presents the voltage-amplifier responsivities (R_v^V). Both figures present the data for both coupled and uncoupled geometries. Note that for comparison purposes, we also refer to prior measurements of the coupled geometry with a voltage follower using the same pyroelectric crystals (detailed in Ref. 6). This systematic comparison permits an evaluation of how thermal coupling (coupled vs uncoupled) and amplifier type (current vs voltage) collectively influence detector's responsivity. All devices demonstrate

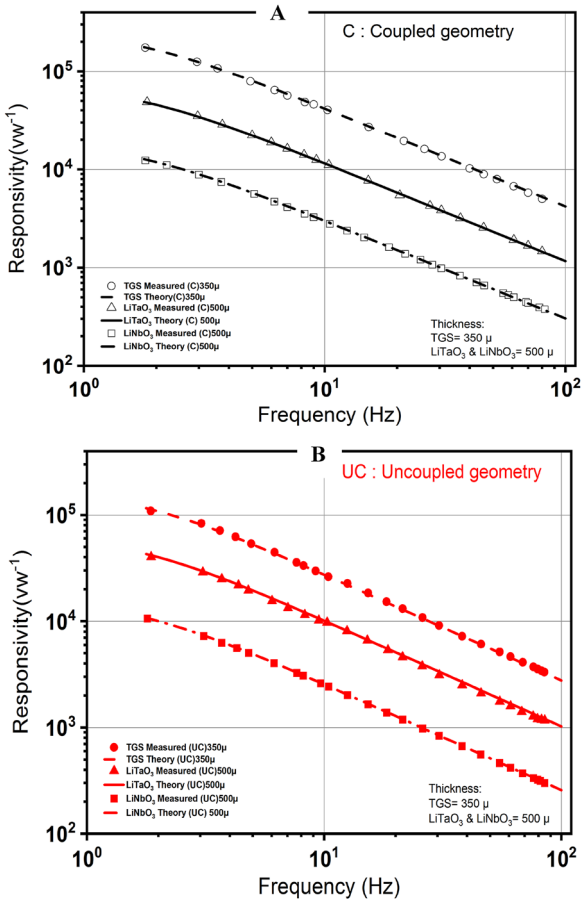


FIG. 5. Comparison of measured current responsivities R_v^i of pyroelectric devices with the theoretically calculated values for $LiTaO_3$, $LiNbO_3$, and TGS as the active materials, for various chopping frequencies at fixed incident radiation power in (A) coupled (C) and (B) uncoupled (UC) geometry.

significant x-ray responses, particularly at low chopping frequencies. The theoretically calculated responsivities are also included in Figs. 4 and 5.

From the above-mentioned figures, our observations are as follows: (1) It is clear that responsivities decrease with increasing frequency in all cases, following approximately a 1/f relationship above about 3 Hz for the current amplifiers and 10 Hz for the voltage amplifiers. This behavior aligns with the expected behavior of the detectors predicted from the models and the turnover frequencies predicted from the τ_E and τ_T values presented in Table I.[24,46,47] In the case of the R_v^i frequency responses, the predicted value of f_c at 1.6 Hz lies just below the lowest measurement frequency of 2 Hz, but the tendency of the response to roll-off below 1.6 Hz is just visible at the lowest frequencies. In the case of the R_v^V frequency responses, the values of f_E for the LN, LT, and TGS devices are 3.7, 3.2, and 3 Hz, respectively, and these turn-over frequencies are clearly visible on the plots. Thus, we can say for the thicker crystals, the frequency response for both current and

08 December 2025 10:51:56

© Author(s) 2025

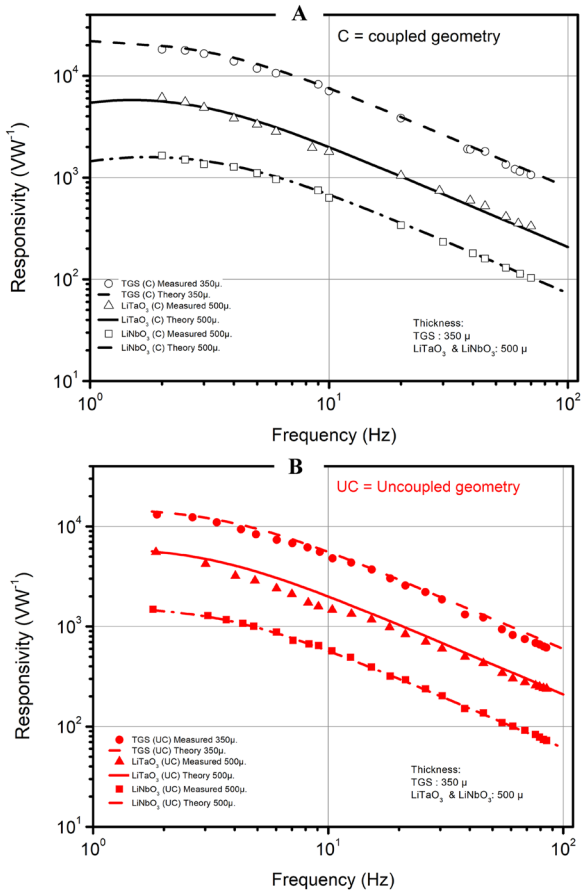


FIG. 6. Voltage responsivities R_v^V of pyroelectric devices with the theoretically calculated values for $LiTaO_3$, $LiNbO_3$, and TGS as the active materials, for various chopping frequencies at fixed incident radiation power in (A) coupled and (B) uncoupled geometry.

voltage amplified devices is dominated by the corresponding electrical time constants. (2) Coupled geometries show a trend toward slightly better signal generation than uncoupled geometries at these thicknesses of the pyroelectric materials, although the two geometries give very similar results for the 0.5 mm LT and LN. The difference is most marked for the TGS crystal, for which the response in the coupled geometry is about 30% greater than the uncoupled case. The reason for the difference may be explained through the differences in x-ray absorptivity for the various materials. As has been discussed previously, for both LT and LN, the x-ray energy is absorbed within the top few tens of microns of the crystal. However, in the case of the 0.35 mm TGS crystal, about 60% of the x-ray energy is absorbed in the combination of silver paste electrodes and the crystal itself. If the crystal is hard-mounted to a copper substrate (coupled geometry), it is easy to show that the remainder of the x-ray energy is absorbed in the top 30 μm of the copper, and a substantial amount of that heat energy will heat the TGS, increasing the response. In the uncoupled case, the remaining 40% of the x-ray energy will be transmitted through the element and lost. This is in reasonable agreement with the differences in responsivity between the two configurations for TGS. (3) Current amplifier configurations exhibit considerably longer time constants (see Table I), resulting in lower roll-off frequencies but significantly higher absolute responsivity values (up to 10^5 V/W) due to built-in gain mechanisms. Voltage follower configurations demonstrate shorter time constants and exhibit a region of relatively flat frequency response between 1 and 3 Hz, enabling dynamic measurement applications where signal drift must be minimized. While this flat response region facilitates stable operation in the low-frequency domain, it comes at the expense of absolute responsivity, particularly evident in uncoupled geometry configurations. (4) Among the materials tested, TGS consistently demonstrates superior performance with the highest responsivity, followed by LT and then LN. TGS responsivity is ~5–10 times greater than that of LN. This hierarchy is maintained across all amplifier types and geometries and is in-line with the pyroelectric figures of merit for the materials.[5,24] (5) The excellent agreement between theoretical predictions and experimental measurements across all configurations validates both the theoretical models and experimental methodology employed in this study.

The average variance in R_v^i measurements in the current configuration across the frequency range was less than 1% of the mean.

Following comprehensive responsivity measurements of LT, TGS, and LN pyroelectric crystals in both coupled and uncoupled geometries, LT was selected for detailed optimization due to its advantageous combination of a high pyroelectric coefficient (p = 176 μC m^{-2} K^{-1}), moderate dielectric constant (ε_r = 43.5), and excellent thermal stability under high radiation flux. Although TGS exhibited superior sensitivity, its low Curie temperature (49 °C) and hygroscopic nature may lead to rapid degradation under intense synchrotron radiation. LN, while thermally and chemically robust, consistently showed lower responsivity than LT across all tested configurations. One basic method for improving the response of pyroelectric detectors is to reduce the thickness of the pyroelectric element[48,49] to reduce its thermal capacitance and increase responsivity by increasing the temperature change for a given amount of energy input to the element.[50,51] Reducing element thickness will also change the values of τ_T and τ_E, thus altering the frequency response of the device. The change in τ_T with element thickness is expected to be particularly interesting in the context of coupled and uncoupled thermal geometries, and this effect is discussed in Sec. IV A 2.

2. Thickness-dependence of $LiTaO_3$ response

The current responsivity measurements R_v^i for devices made with LT samples with thicknesses ranging from 100 to 500 μm are shown in Fig. 7 (uncoupled) and Fig. 8 (coupled). The results reveal several important trends. First, above the roll-off frequencies determined by either the electrical or thermal time constants (see Table I), the responsivities decrease with increasing frequency as $1/f$ for all thicknesses and geometries, consistent with theory. Notably, thinner LT crystals (100 μm) demonstrate the highest responsivities at all frequencies, with a progressively decreasing responsivity for the thicker crystals. There is excellent agreement between modeled and

08 December 2025 10:51:56

© Author(s) 2025

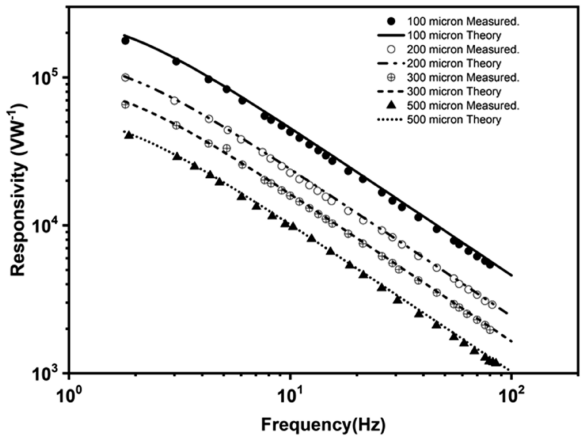


FIG. 7. Voltage responsivities R_v^i of $LiTaO_3$ crystals of different thicknesses for uncoupled geometry, compared with the theoretically calculated values.

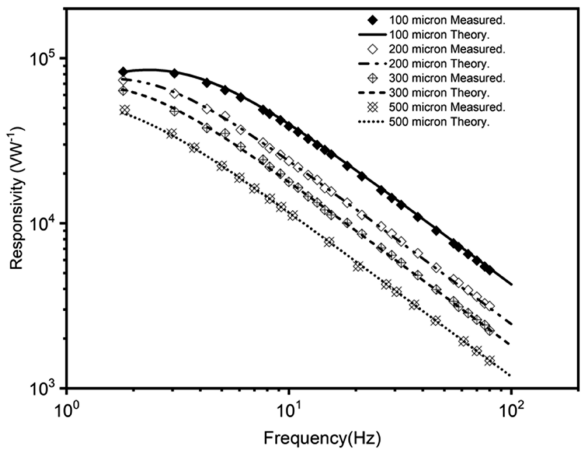


FIG. 8. Voltage responsivities R_v^i of $LiTaO_3$ crystals of different thicknesses for coupled geometry, compared with the theoretically calculated values.

observed responsivities across the full range of frequencies, meaning that the COMSOL calculations of the device thermal characteristics are accurate. In the case of the uncoupled geometry, we can see from Table I that the thermal time constants are all well below 2 Hz, so the frequency response for R_v^i is controlled by an f_c of 1.6 Hz, which is just below the lowest frequency of measurement, but the incipient tendency to roll-off at that frequency is clearly visible, as for the thicker crystals discussed above.

A key observation from the uncoupled geometry (Fig. 6) is that the performance advantage of thinner crystals is more pronounced than the coupled geometry (Fig. 7). This is particularly the case at frequencies below about 5 Hz, especially for the 100 μm thick element. In the uncoupled configuration, better thermal isolation allows the thinner crystal to achieve a greater thermal response and higher responsivity at lower frequencies, as reduced thermal conductance minimizes heat loss to the substrate. This advantage diminishes with increasing crystal thickness. A marked effect visible in the frequency responses of the coupled configuration devices is that for the 100 and 200 μm crystals, the thermal turn-over frequencies f_T of 3.4 and 1.7 Hz, respectively, are clearly visible. It means that for a 100 μm crystal, below about 5 Hz, the uncoupled configuration has a distinct performance advantage, giving a responsivity that is about double that of the coupled configuration.

This thickness-dependent study highlights a key practical consideration relevant to synchrotron-based x-ray detection using pyroelectrics. Thinner LT crystals in the uncoupled geometry exhibit superior responsivity ideal for applications requiring high sensitivity such as medical imaging and spectroscopy.[52] In contrast, thicker LT crystals have longer thermal time constants and a responsivity ~10% lower than that of the 100 μm crystals at 10 Hz and about one-half the response at 2 Hz. These findings are validated by close agreement between experimental data and theoretical predictions. A numerical comparison of responsivities measured in both the geometries for various thicknesses is given in Table S3 of the supplementary material.

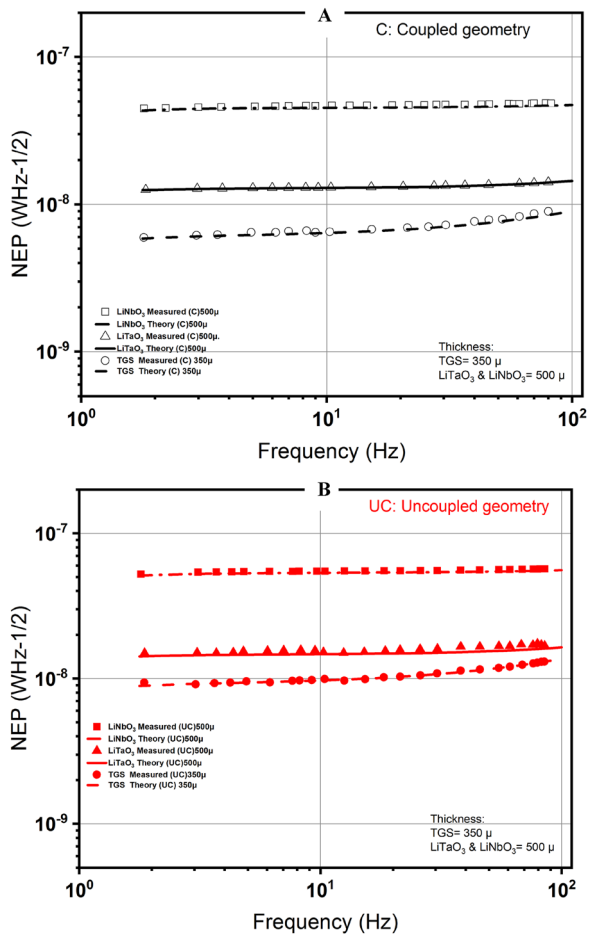


FIG. 9. Frequency-dependent NEP comparison between experimental and theoretical values for $LiTaO_3$, $LiNbO_3$, and TGS at various chopping frequencies in (A) coupled and (B) uncoupled geometry with current amplifier.

08 December 2025 10:51:56

© Author(s) 2025

B. Noise equivalent power (NEP)

1. For different pyroelectric materials

NEP measurements were conducted as functions of frequency for both coupled and uncoupled geometries, as well as for current amplifier and voltage follower configurations. The NEP performances of devices using the three thicker TGS, LN, and LT pyroelectric elements in the current amplifier configuration were compared between the coupled geometry and the uncoupled geometry (Fig. 9). For these relatively thick elements, the coupled geometry configuration demonstrates consistently lower NEP values across all three materials than the uncoupled configuration, indicating superior detection sensitivity. This performance advantage is particularly evident for TGS, which exhibits the lowest NEP values (~6.50×10^{-9} W/$\sqrt{}$Hz in coupled geometry compared to 9.70×10^{-9} W/$\sqrt{}$Hz at 10 Hz in uncoupled geometry) across the measured frequency range. The relative performance ranking of materials remains consistent in both configurations, with TGS showing the lowest NEP values, followed by $LiTaO_3$ in the middle range, and $LiNbO_3$ displaying the highest NEP values. All materials show a slight increase in NEP with increasing frequencies, which aligns with theoretical expectations.

Comparing the uncoupled geometry in current amplifier configuration [Fig. 9 (UC)] vs voltage follower configuration (Fig. 10) reveals substantial differences in detector performance. The voltage follower configuration exhibits significantly higher NEP values (i.e., lower performance) by approximately one order of magnitude across all three materials. Specifically, in the current amplifier configuration, NEP values range from ~10^{-9} to 10^{-8} W/$\sqrt{}$Hz, while in the voltage follower configuration, they range from ~10^{-8} to 10^{-7} W/$\sqrt{}$Hz. In addition, the frequency response characteristics differ between the two configurations, with the voltage follower showing a flatter frequency response than the more frequency-dependent behavior observed in the current amplifier configuration. This difference can be attributed to how each configuration handles the pyroelectric current generated by the detector elements. In voltage follower configurations, additional noise sources may be introduced due to the high input impedance required, while current amplifiers can more efficiently process the pyroelectric current signals generated by temperature fluctuations. Despite these differences, the relative performance ranking of materials remains consistent, with TGS continuing to demonstrate the lowest NEP values, followed by $LiTaO_3$ and $LiNbO_3$ in both configurations.

2. Thickness-dependence of $LiTaO_3$ NEP

NEP measurements for $LiTaO_3$ pyroelectric elements of varying thicknesses (100, 200, 300, and 500 μm) in coupled and uncoupled geometries using current amplifier configuration are shown in Fig. 11. In both geometries, there is a clear thickness-dependent performance trend, with thinner elements consistently demonstrating superior detection sensitivity. The 100 μm element exhibits the lowest NEP values (~5.4×10^{-9} W/$\sqrt{}$Hz at 10 Hz frequencies), while the 500 μm element shows the highest NEP values (~1.3×10^{-8} W/$\sqrt{}$Hz) across the measured frequency range. The close agreement

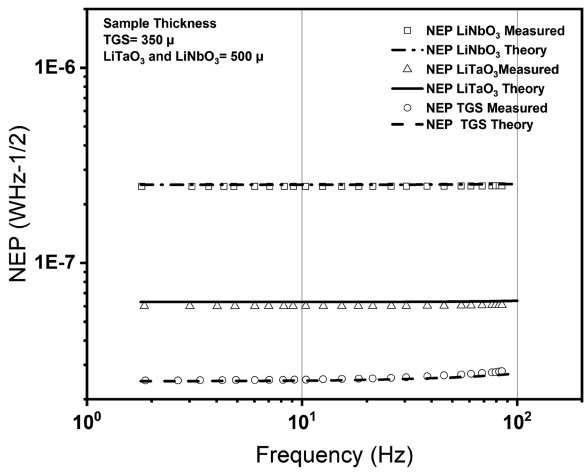


FIG. 10. NEP for voltage amplifier in uncoupled geometry for $LiTaO_3$, $LiNbO_3$, and TGS at various chopping frequencies.

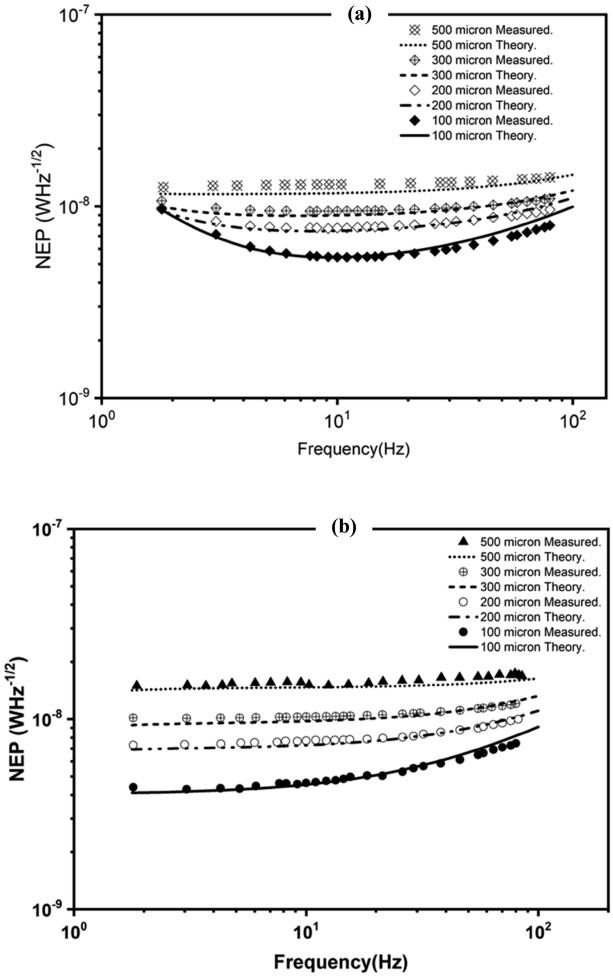


FIG. 11. Frequency-dependent NEP comparison between experimental and theoretical values for $LiTaO_3$ crystal for (a) coupled geometry and (b) uncoupled geometry with current amplifier.

08 December 2025 10:51:56

© Author(s) 2025

between experimental data and theoretical predictions in both configurations confirms the validity of the underlying physical models used to characterize these pyroelectric systems.

A key difference between the coupled and uncoupled geometries lies in their frequency response characteristics. The coupled geometry [Fig. 11(a)] exhibits a distinctive "U-shaped" frequency response curve, particularly for the thinner elements, with minimum NEP values occurring in the mid-frequency range (~5–10 Hz). This effect reflects the values of the thermal turnover frequencies for the thinnest coupled LT crystals, as discussed above. This suggests an optimal operating frequency range where thermal noise contributions are minimized. In contrast, the uncoupled geometry [Fig. 11(b)] displays a more monotonic frequency response, with NEP values gradually increasing with frequency across all thickness values. This difference indicates that the thermal boundary conditions significantly affect the frequency-dependent noise characteristics of the pyroelectric elements. While both configurations maintain the same general thickness-dependent performance trend, the uncoupled geometry provides performance that is more predictable across the frequency spectrum, which may be advantageous for applications requiring consistent response over wide frequency ranges. The coupled geometry, however, might offer slightly better performance at specific operating frequencies, potentially beneficial for narrowband detection applications.

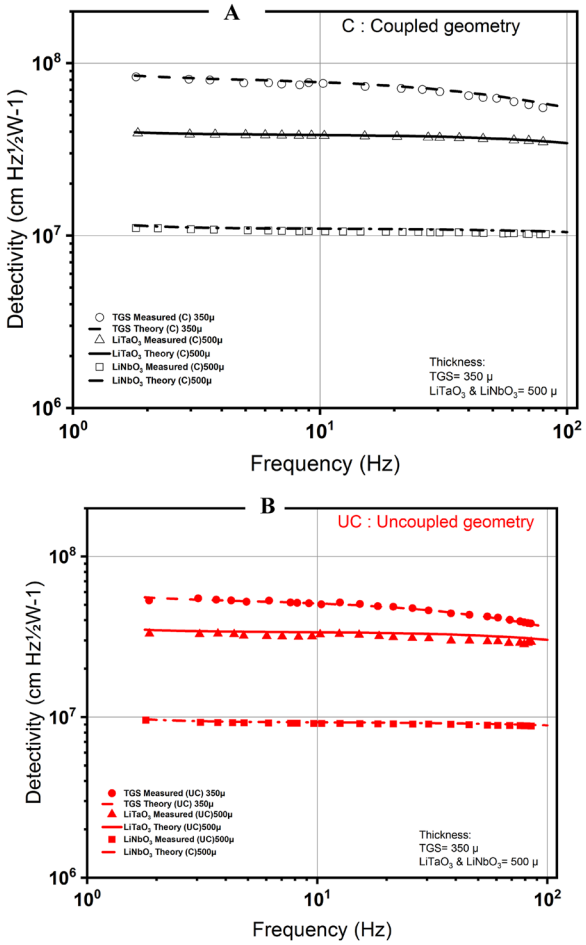


FIG. 12. Comparison of special detectivity of pyroelectric crystal in (A) coupled and (B) uncoupled geometry with theoretically calculated values for $LiTaO_3$, $LiNbO_3$, and TGS as pyroelectric crystal for various chopping frequencies at fixed incident radiation power.

C. Specific detectivity (D*)

1. For different pyroelectric materials

The detectivity performances of the different pyroelectric materials (TGS, LT, and LN) using the thickest elements across various configurations were evaluated both experimentally and theoretically, as shown in Fig. 12 (current amplifier) and Fig. 13 (voltage follower amplifier).

In both uncoupled and coupled geometries using current amplifier configuration, TGS consistently demonstrates superior detectivity (~5×10^7 cm $Hz^{1/2}$ W^{-1}), ~5–7 times higher than that of $LiTaO_3$ (~3×10^7 cm $Hz^{1/2}$ W^{-1}), while $LiNbO_3$ shows the lowest values (~1×10^7 cm $Hz^{1/2}$ W^{-1}). Both geometries show a similar trend of slight detectivity decrease at higher frequencies, particularly for TGS, although this frequency dependence is minimal for $LiNbO_3$. The relative performance ranking of these materials remains consistent regardless of the geometric configuration, suggesting that material properties rather than geometry dominate detectivity performance in current amplifier setups.

When comparing the current amplifier [Fig. 12 (UC)] with voltage follower configuration (Fig. 13) for uncoupled geometry, there is a notable difference in absolute detectivity values. The voltage follower configuration shows lower detectivity values approximately by an order of one magnitude across all materials than the current amplifier setup. Specifically, in the voltage follower configuration, TGS exhibits detectivity of around 2×10^7 cm $Hz^{1/2}$ W^{-1}, $LiTaO_3$ exhibits detectivity of around 8×10^6 cm $Hz^{1/2}$ W^{-1}, and $LiNbO_3$ ~2×10^6 cm exhibits detectivity of $Hz^{1/2}$ W^{-1}. While the

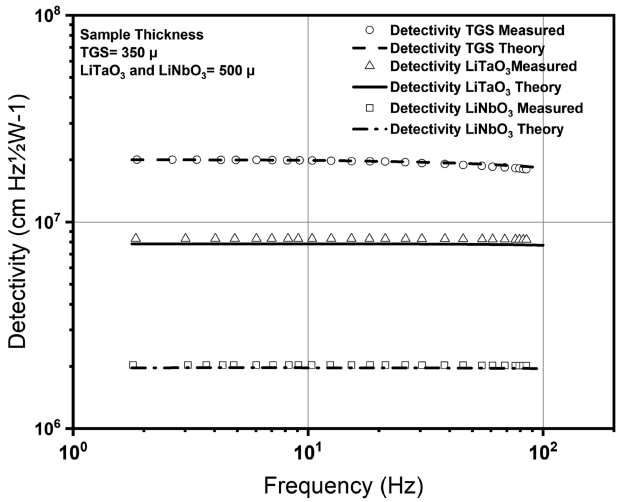


FIG. 13. Comparison of special detectivity of pyroelectric crystal in uncoupled geometry with voltage follower amplifier and compared with theoretically calculated value for $LiTaO_3$, $LiNbO_3$, and TGS as pyroelectric crystal.

08 December 2025 10:51:56

© Author(s) 2025

current amplifier configuration shows more pronounced frequency dependence (particularly for TGS), the voltage follower configuration demonstrates more stable detectivity values across the entire frequency range, suggesting it might offer more consistent performance in applications requiring uniform response across various frequencies. Despite these differences, the relative performance hierarchy of the materials remains unchanged, with TGS consistently outperforming the others in both configurations.

The supplementary material (Tables S1 and S2) summarizes key parameters (e.g., D^* and NEP) at 10 and 80 Hz for both geometries at room temperature, reinforcing the consistency between experimental and theoretical results under varying operational conditions. The responsivity error stays below 5% across all configurations, indicating good agreement with theory in the current amplifier. A significant improvement (~4.8 times) in detectivity is observed when switching from voltage amplifier to current amplifier configuration.

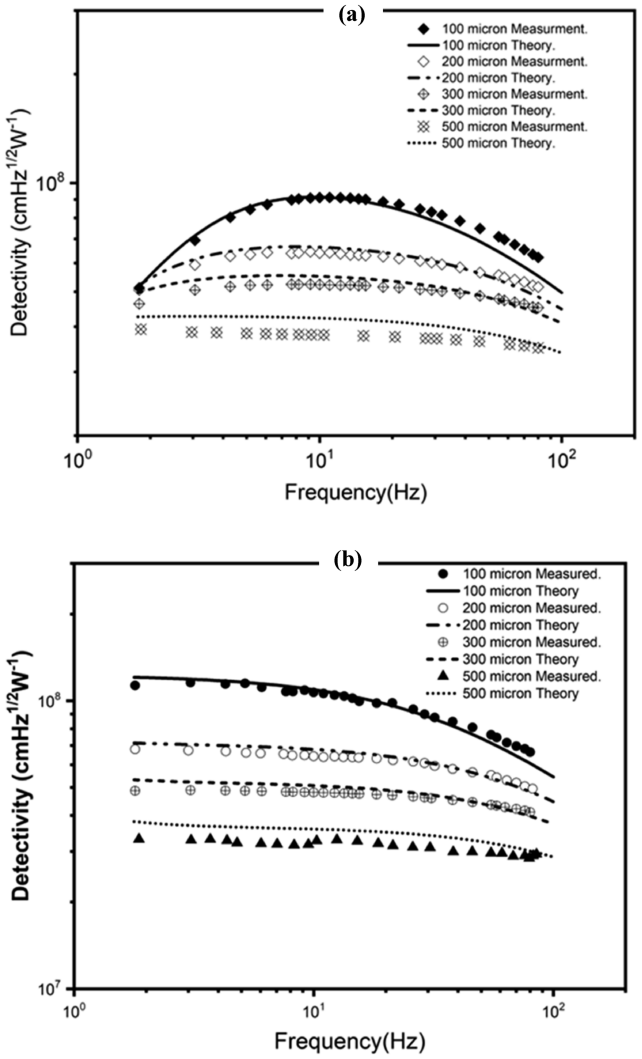


FIG. 14. Specific detectivity of LiTaO3 based detectors for (a) coupled and (b) uncoupled geometries for various thicknesses using current amplifier.

2. For thickness-dependence of $LiTaO_3$

Figure 14 shows the detectivity of the $LiTaO_3$ pyroelectric detector at various thicknesses in coupled and uncoupled geometry using a current amplifier.

The coupled geometry [Fig. 14(a)] exhibits a distinct bell-shaped frequency response with peak detectivity occurring around 5–10 Hz before gradually declining at higher and lower frequencies. In contrast, the uncoupled geometry [Fig. 14(b)] demonstrates more consistent detectivity values at lower frequencies (1–10 Hz) followed by a more gradual decline at higher frequencies. Notably, the uncoupled configuration consistently achieves higher absolute detectivity values across all thicknesses, and the 100 μm elements reach ~1.1×10^8 cm $Hz^{1/2}$ W^{-1} in uncoupled geometry vs about 9×10^7 cm $Hz^{1/2}$ W^{-1} in coupled geometry at 10 Hz. Both configurations show excellent agreement between theoretical predictions and experimental measurements, with thinner elements consistently outperforming thicker ones. Detectivity drops as thickness increases. This behavior aligns with general findings in detector physics, where increased thickness can improve absorption but often at the cost of slower response and reduced detectivity due to increased noise and thermal inertia.[53,54] The supplementary material (Table S3) summarizes key parameters (e.g., D^* and NEP) at 10 and 80 Hz for both geometries at room temperature, reinforcing the consistency between experimental and theoretical results under varying operational conditions. Both geometries (coupled and uncoupled) show good agreement (errors <2%), but uncoupled geometry presents a slightly larger scatter in terms of responsivity, whereas detectivity aligns very well in both cases (errors ~1%), although with moderate scatter.

V. CONCLUSION

This investigation demonstrates significant advances in pyroelectric detector optimization for synchrotron x-ray applications through systematic variation in material properties, thermal geometries, and readout electronics. Current amplification consistently outperformed voltage follower configurations across all tested materials and geometries, with improvements in detectivity approaching five-fold. While TGS exhibited the highest responsivity and lowest NEP among tested materials, practical considerations favor $LiTaO_3$ for its superior thermal stability and reliability under intense synchrotron radiation.

The thickness-dependent studies of $LiTaO_3$ reveal a clear inverse relationship between crystal thickness and detector performance, with 100 μm elements achieving detectivity values exceeding 10^8 cm $Hz^{1/2}$ W^{-1}, representing a significant improvement over previously reported results. The observed performance enhancements were consistent with theoretical predictions based on thermal and electrical modeling, validating our approach to detector optimization.

Thermal geometry proved crucial to performance optimization, with uncoupled configurations particularly advantageous for

08 December 2025 10:51:56

© Author(s) 2025

thinner elements at lower frequencies, where thermal isolation maximizes temperature fluctuations, while coupled geometries offer more consistent frequency response characteristics beneficial for broadband applications. The close agreement between experimental results and theoretical predictions across all configurations provides a robust foundation for future device engineering.

These findings establish pyroelectric detectors as viable alternatives for synchrotron beam intensity measurement and spectroscopy applications, particularly where conventional detectors face limitations such as flux saturation, cooling requirements, or non-requirement of spectroscopic energy resolution. The strategic combination of material selection, geometric configuration, and readout electronics enables optimization for specific synchrotron measurement scenarios, including high-flux beam characterization, time-resolved intensity monitoring, and applications requiring radiation-hard detectors. Comparison of the various detectors that are extensively used in synchrotron application are compared and given in the supplementary material.

SUPPLEMENTARY MATERIAL

See the supplementary material for detailed preamplifier circuit design using the ADA4530-1 transimpedance amplifier and comprehensive performance data tables for TGS, $LiTaO_3$, and $LiNbO_3$ pyroelectric x-ray detectors in synchrotron beamline applications. It also includes comparison of the various detectors that are extensively used in synchrotron application.

ACKNOWLEDGMENTS

The authors thank Dr. M. K. Tiwari and Dr. Archna Sagdeo for their help in discussion, and Dr. Norbert Neumann and InfraTec GmbH for providing the thin $LiTaO_3$ samples.

AUTHOR DECLARATIONS

Conflict of Interest

The authors have no conflicts to disclose.

Author Contributions

S. R. Kane: Conceptualization (lead); Formal analysis (lead); Investigation (lead); Methodology (lead); Resources (lead); Validation (lead); Writing – original draft (lead); Writing – review & editing (lead). **R. W. Whatmore**: Conceptualization (equal); Data curation (equal); Formal analysis (equal); Methodology (equal); Project administration (equal); Supervision (equal); Writing – original draft (equal); Writing – review & editing (equal). **P. K. Jha**: Conceptualization (supporting); Investigation (supporting); Project administration (equal); Supervision (equal); Writing – original draft (supporting); Writing – review & editing (supporting). **P. K. Mehta**: Conceptualization (supporting); Investigation (supporting); Project administration (supporting); Writing – original draft (supporting); Writing – review & editing (supporting).

DATA AVAILABILITY

The data that support the findings of this study are available within the article and its supplementary material.

REFERENCES

[1] P. Willmott, *An Introduction to Synchrotron Radiation: Techniques and Applications* (John Wiley and Sons, Ltd., 2011).
[2] *Synchrotron Radiation in Materials Science*, edited by C. Fan and Z. Zhao (Wiley-VCH Verlag GmbH, 2018).
[3] A. Niculae, S. Aschauer, M. Bornschlegl, K. Hermenau, L. Strüder *et al.*, "Latest improvements on silicon drift detectors for fast, high resolution EDX spectroscopy in electron microscopy," Microsc. Microanal. **29**, 2087–2088 (2023).
[4] C. Collins, N. Rowlands, P. Statham, and J. Holland, "New large area silicon drift detectors – Fast analysis without compromise," Microsc. Today **17**, 6–11 (2009).
[5] R. W. Whatmore, "Pyroelectric devices and materials," Rep. Prog. Phys. **49**, 1335–1386 (1986).
[6] S. R. Kane, R. W. Whatmore, M. N. Singh, S. Satapathy, P. K. Jha, and P. K. Mehta, "Characterizing pyroelectric detectors for quantitative synchrotron radiation measurements," Sens. Actuators, A **387**, 116406 (2025).
[7] Y. Ta, "Action of radiations on pyroelectric crystals," Compt. Rend. **207**, 1042–1044 (1938).
[8] J. H. Ludlow, W. H. Mitchell, E. H. Putley, and N. Shaw, "Infra-red radiation detection by the pyroelectric effect," J. Sci. Instrum. **44**, 694–696 (1967).
[9] R. W. Astheimer and F. Schwarz, "Thermal imaging using pyroelectric detectors," Appl. Opt. **7**, 1687–1695 (1968).
[10] R. Watton, "Ferroelectric materials and devices in infrared detection and imaging," Ferroelectrics **91**(1), 87–108 (1989).
[11] S. R. Kane, M. N. Singh, S. Satapathy, P. K. Mehta, P. K. Jha, and R. R. Urkude, "Extended X-ray absorption fine structure (EXAFS) measurement of Cu metal foil using thermal wave detector: A comparative study," Nucl. Instrum. Methods Phys. Res., Sect. A, **1016**, 169066 (2024).
[12] D. L. Hester, D. D. Glower, and L. J. Overton, "Use of ferroelectrics for gamma-ray dosimetry," IEEE Trans. Nucl. Sci. **11**, 145–154 (1964).
[13] L. S. Kremenchugskii and R. Y. Strakovskaya, "Using pyroelectric detectors for the dosimetry of pulsed γ radiation," Sov. At. Energy **41**, 813–817 (1976).
[14] A. A. de Carvalho, A. L. Brassalotti, M. H. de Paula, and A. J. Alter, "Use of lithium niobate detector for measuring X-ray intensity in mammographic range," Electron. Lett. **40**, 1097–1098 (2004).
[15] W. K. Sakamoto, G. P. Estevam, A. A. de Carvalho, W. Pontes, and M. H. de Paula, "Pyroelectric composite film for X-ray intensity detection," Mater. Res. **15**, 198–203 (2012).
[16] J. Kawai, H. Ida, H. Murakami, and T. Koyama, "X-ray fluorescence analysis with a pyroelectric x-ray generator," X-Ray Spectrom. **34**, 521–524 (2005).
[17] J. A. Geuther and Y. Danon, "High-energy x-ray production with pyroelectric crystals," J. Appl. Phys. **97**, 104916 (2005).
[18] S. Mohtashami, H. Afarideh, and K. Moshkbar-Bakhshayesh, "Pyroelectric crystals for generation of neutrons: A review," J. Appl. Phys. **135**, 200701 (2024).
[19] R. Mondal, M. A. M. Hasan, J. M. Baik, and Y. Yang, "Advanced pyroelectric materials for energy harvesting and sensing applications," Mater. Today **66**, 273–301 (2023).
[20] E. W. Yap, N. Kumar, D. Damjanovic, R. M. Preston, and J. E. Daniels, "Pyroelectric material property considerations for x-ray generation," J. Appl. Phys. **131**(11), 114503 (2022).
[21] A. Rogalski, *Infrared Detectors* (CRC Press, 2011).
[22] J. Fraden, *Handbook of Modern Sensors: Physics, Designs, and Applications* (Springer International Publishing, 2016).
[23] M. Chirtoc, E. H. Bentefour, J. S. Antoniow, C. Glorieux, J. Thoen, S. Delenclos, A. H. Sahraoui *et al.*, "Current mode versus voltage mode measurement of signals from pyroelectric sensors," Rev. Sci. Instrum. **74**, 648–650 (2003).
[24] R. W. Whatmore and S. J. Ward, "Pyroelectric infrared detectors and materials—A critical perspective," J. Appl. Phys. **133**, 080902 (2023).

08 December 2025 10:51:56

© Author(s) 2025

[25]J. B. Robertson and R. K. Crouch, "Evaluation of commercial pyroelectric detectors," NASA TM X-74024, 1977.
[26]S. G. Porter, "A brief guide to pyroelectric detectors," Ferroelectrics **33**, 193–206 (1981).
[27]J. Jirmann, "Optimized preamplifiers for pyroelectric detectors," Int. J. Infrared Millimeter Waves **6**(11), 1091–1101 (1985).
[28]P. Muralt, "Micromachined infrared detectors based on pyroelectric thin films," Rep. Prog. Phys. **64**, 1339–1388 (2001).
[29]R. N. Schouten, "A new amplifier design for fast low-noise far-infrared detectors using a pyroelectric element," Meas. Sci. Technol. **9**(4), 686–691 (1998).
[30]E. H. Putley, "The applications of pyroelectric devices," Ferroelectrics **33**, 207–216 (1981).
[31]Z. Liang, S. Li, Z. Liu, Y. Jiang, W. Li, T. Wang, and J. Wang, "High responsivity of pyroelectric infrared detector based on ultra-thin (10 μm) $LiTaO_3$," J. Mater. Sci.: Mater. Electron. **26**, 5400–5404 (2015).
[32]G. Hyseni, N. Caka, and K. Hyseni, "Infrared thermal detectors parameters: Semiconductor bolometers versus pyroelectrics," WSEAS Trans. Circuits Syst. **9**, 238–247 (2010).
[33]Z. Bielecki and M. Brudnowski, "Method of popcorn-noise reduction," Opto-Electron. Rev. **11**, 45–50 (2003).
[34]L. E. Garn, "Fundamental noise limits of thermal detectors," J. Appl. Phys. **55**, 1243–1253 (1984).
[35]Laser Components, "IR detector," available at: https://www.lasercomponents.com/ww/product/one-channel-litao3-pyroelectric-detector/.
[36]InfraTec, "IR sensors," available at: https://www.infratec.eu/sensor-division/pyroelectric-detectors/.
[37]N. Bennaji, I. Mellouki, and N. Yaco, "Determination of thermal properties of graphite-black-coating by photothermal and electro-pyroelectric techniques," Sens. Transducers **27**, 75–81 (2014).
[38]R. Lehmkau and J. Lienig, "A novel approach to model the thermal-electrical behavior of pyroelectric infrared sensors," in SMSI 2021 Conference – Sensor and Measurement Science International, 2021.
[39]C. C. Chang, K. P. Chu, and Y. C. Lai, "The characterization and fabrication of pyroelectric infrared sensor," Tamkang J. Sci. Eng. **8**, 203–206 (2005).
[40]F. Cook, R. Lord, G. Sitbon, A. Stephens *et al.*, "A pyroelectric thermal sensor for automated ice nucleation detection," Atmos. Meas. Tech. **13**, 2785–2795 (2020).
[41]J.-J. Ho, Y. K. Fang, W. J. Lee, F. Y. Chen, W. T. Hsieh *et al.*, "The dynamic response analysis of a pyroelectric thin-film infrared sensor with thermal isolation improvement structure," IEEE Trans. Electron Devices **46**, 2289–2294 (1999).
[42]S. R. Kane, A. K. Sinha, A. K. Singh, and S. Kumar, "Experimental setup to measure thermal waves generated by X-ray absorption using pyroelectric sensor," Rev. Sci. Instrum. **90**, 033301 (2019).
[43]A. K. Sinha, A. Sagdeo, P. Gupta, A. Upadhyay, A. Kumar, M. N. Singh, R. K. Gupta, S. R. Kane, A. Verma, and S. K. Deb, "Angle dispersive X-ray diffraction beamline on Indus-2 synchrotron radiation source: Commissioning and first results," J. Phys.: Conf. Ser. **425**, 072017 (2013).
[44]S. K. Deb, G. Singh, and P. D. Gupta, "Indus-2 synchrotron radiation source: Current status and utilization," J. Phys.: Conf. Ser. **425**, 072009 (2013).
[45]V. Wong, "Analog devices," available at: https://www.analog.com/en/resources/app-notes/an-1373.html.
[46]A. Hossain and M. H. Rashid, "Pyroelectric detectors and their applications," IEEE Trans. Ind. Appl. **27**, 824 (1991).
[47]I. Lubomirsky and O. Stafsudd, "Invited Review Article: Practical guide for pyroelectric measurements," Rev. Sci. Instrum. **83**, 051101 (2012).
[48]V. Stenger, M. Shnider, S. Sriram, D. Dooley, M. Stout, L. P. Sadwick, and C. M. O'Sullivan, "Thin Film Lithium Tantalate (TFLT) pyroelectric detectors," Proc. SPIE **8261**, 82610Q (2012).
[49]T. Liang, S. J. Lin, Y. Li, C. Lei, and C. Y. Xue, "Research on the effect of mechanical processing on lithium tantalate crystal pyroelectric coefficient," Adv. Mater. Res. **834–836**, 880–884 (2013).
[50]V. Norkus, J.-P. Chatard, and P. N. J. Dennis,"Detectors and associated signal processing," in *SPIE Optical Systems Design* (SPIE, St Etienne France, 2004).
[51]J. Si, X. Xiao, Y. Zhang, Y. Huang *et al.*, "Pyroelectric properties and applications of lithium tantalate crystals," Crystals **14**, 579 (2024).
[52]X. Hou, Y. Liu, S. Bai, S. Yu *et al.*, "Pyroelectric photoconductive diode for highly sensitive and fast DUV detection," Adv. Mater. **36**, 2314249 (2024).
[53]L. R. MacDonald, W. C. J. Hunter, P. E. Kinahan, and R. S. Miyaoka, "Effects of detector thickness on geometric sensitivity and event positioning errors in the rectangular PET/X scanner," IEEE Trans. Nucl. Sci. **60**, 3242–3252 (2013).
[54]H. Saddam, S. Zhao, Q. Zhang, and L. Tao, "Comparative analysis of thin and thick $MoTe_2$ photodetectors: Implications for next-generation optoelectronics," Nanomaterials **22**, 1804 (2024).

08 December 2025 10:51:56

© Author(s) 2025